nature portfolio

Peer Review File

Machine Learning Driven Discovery of Low Modulus Biomedical Titanium Alloys for Additive Manufacturing

Corresponding Author: Dr Swee Leong Sing

This file contains all reviewer reports in order by version, followed by all author rebuttals in order by version.

Version 0:

Reviewer comments:

Reviewer #1

(Remarks to the Author)
The authors presented a machine-learning (ML)-driven computational framework for discovering AM-specific biomedical β-Ti alloy compositions with desired properties, and performed experimental validation to efficiently develop biomedical Ti-15.8Nb-9.2Ta-10.0Zr-7.7Sn alloy. It is considered after major revisions required, and the following points should be considered.
1. What is the actual use of the newly developed biomedical β-Ti alloy? It is noted that different service environment and requirements should be selected for evaluation of orthopaedic and dental materials. Please present the research objective in the section Introduction. If the present Ti alloy is designed for the development of artificial joint, the Co-Cr-based alloys should be used for comparisons.
2. How to calculate the non-equilibrium solidification behaviour including growth restriction factor (GRF), solidification freezing range (SFR), and hot-cracking susceptibility (HCS)? The calculated values of Ti-15.8Nb-9.2Ta-10.0Zr-7.7Sn and Ti64 alloys should be used to compare with the experimental results, which can support that the GRF, SFR, and HCS values can be used for prediction of printability.
3. Please provide the data used in the ML calculation for verification.
4. The authors used a 3.5 wt.% NaCl solution for the corrosion tests. Generally, electrochemical corrosion measurements of biomedical materials are performed in the 0.9 wt.% NaCl solution, instead of 3.5 wt.% NaCl solution. Please give the experimental results in the 0.9 wt.% NaCl solution.
5. The relationship among the YS, SFR, Ip, HCS, and BF is very complex, not simple linear. Therefore, I cannot understand the objective functions to maximise YS, SFR, and Ip, and to minimize HCS and BF in the multi-objective optimisation. Please explain it.
6. The Ti-15.8Nb-9.2Ta-10.0Zr-7.7Sn alloy has higher corrosion-current density than Ti64 alloy. Does this result indicate that the ML calculations fail in the corrosion property? Maybe the electrochemical impedance spectroscopy test can be performed for these two alloys.

Reviewer #2

(Remarks to the Author)
This work presents a machine-learning (ML)-driven computational framework for discovering AM-specific biomedical β-Ti alloy compositions with low-modulus, optimized printability, mechanical and corrosion properties, and biocompatibility. Using this framework, a new AM-specific Ti-Nb-Ta-Zr-Sn (ANTZS) alloy was correspondingly designed and validated via laser powder bed fusion (LPBF). The manuscript is very well organized and well written. While the concept of machine learning has been reported in the literature, preparing medical metals for 3D printing is still novel. Please find my comments as follow:
1. BF is suitable for predicting the elastic modulus of β-titanium alloys, but not for all medical metal materials. The framework can be just used to design 3D β-titanium alloys with low elastic modulus. So, I suggest the author consider optimizing the title of manuscript.
2. The author mentioned “The alloy composition sets include Ti as the base element, with Nb and Ta varying from 0 to 30 wt.% (in increments of 6 wt.%), and Zr and Sn varying from 0 to 10 wt.% (in increments of 5 wt.%).”, Why set such a component interval?
3. Generally speaking, the larger the SFR is, the more likely solidification cracks occur. In the model of this article, how to balance the contradiction between nucleation rate and cracks?

4. In section 2.3, where are the objective functions YS, SFR, lp, HCS and BF? Where is GRF?
5. What do the color gradations in Figures 4a and 4b represent? Porosity?
6. Please provide the experimental evidence of ANTZS alloy with a smaller melt pool and smaller mushy zone compared to Ti64. What are the reasons for this phenomenon to occur?
7. The arrows in Figure 4i were not the Fusion Line. Please use an arrow to indicate the β-grains.
8. Is the external force of the tensile test applied parallel to the building direction or perpendicular to the printing direction?
9. After the ML calculation, the author chosen one ANTZS composition to conduct the verification experiments, how did the authors balance printability and performance? Just chose one composition to conduct the verification experiments, is the quantity too small?
10. Why was Ti6Al4V used for comparison in this study instead of other beta titanium alloys?
11. There are two (C) in the title of Figure 4.
12. Why does the as-cast alloy undergo a phase transformation during the tensile, while the printed alloy does not? Is there a significant difference in the elastic modulus between the two alloys?

Version 1:

Reviewer comments:

Reviewer #1

(Remarks to the Author)
The revision can be accepted.

(Remarks on code availability)

Reviewer #2

(Remarks to the Author)
The author answered almost all of my questions carefully, but there are two questions that need to be explained by the author before acceptance.
1. In the revised paper, the authors mentioned “During tensile test, it can be induced that the softer α″ phase deforms and/or reorient first, followed by cooperative deformation and strain-induced β→α″ martensitic transformation, leading to the double-yielding behavior.” In fact, the elastic modulus of α″ is always higher than that of β, so α″ is not the softer. Moreover, before the first yielding, when stress is applied to both the β phase and the α″ phase simultaneously, the deformation of the α″ phase is smaller due to the higher elastic modulus of the hardened phase. From the moment of yielding, the martensitic phase transformation begins to activate. Why does the α″ phase deform and/or reorient first?
2. Authors also mentioned “Regarding the elastic modulus, the LPBF-built alloy exhibits a slightly lower modulus compared to the as-cast counterpart (Supplementary Table S4). This difference can be mainly attributed to the pronounced //BD texture in the LPBF sample, which corresponds to a lower modulus direction in the cubic lattice due to weaker atomic bonding.” Elastic modulus is crucial for biomedical materials, but the interpretation of elastic modulus in as-cast and LPBE alloys is still insufficient. Besides the texture, the phase composition, β, and porosity of LPBF alloys also affect the elastic modulus, compared to as-cast alloys, β+α″. Please provide a more complete explanation.

(Remarks on code availability)

Version 2:

Reviewer comments:

Reviewer #2

(Remarks to the Author)
Reviewer’s Comments to NCOMMS-25-48046B
Dear Editor,
In the previous round of review, I raised several concerns regarding data presentation and the depth of mechanistic discussion. In the revised manuscript, the authors have addressed these issues comprehensively and provided clear and detailed responses to all comments.
Overall, my concerns have been adequately resolved, and the manuscript has been substantially improved. I therefore consider that it now meets the standards for publication and recommend its acceptance.

(Remarks on code availability)

Response to the Reviewers' Comments

Title: *Machine Learning-Driven Discovery of Advanced Biomedical Titanium Alloys for Additive Manufacturing*

Manuscript number: *NCOMMS-25-48046A*

First of all, we would like to thank the Reviewers for their constructive comments & suggestions, which have substantially improved the quality and clarity of our work. In response, we have carefully revised the manuscript to address each point raised. All revised parts have been highlighted in yellow in the revised manuscript.

Reviewer #1

General comment:

The authors presented a machine-learning (ML)-driven computational framework for discovering AM-specific biomedical β-Ti alloy compositions with desired properties, and performed experimental validation to efficiently develop biomedical Ti-15.8Nb-9.2Ta-10.0Zr-7.7Sn alloy. It is considered after major revisions required, and the following points should be considered.

Response:

We sincerely thank the Reviewer for the valuable and constructive comments. In response, we have conducted additional experiments (for example, conducting the electrochemical measurement in the 0.9 wt.% NaCl solution), and expanded the relevant discussions to clarify the objectives and methodological details of the alloy design framework, etc. We hope that our responses and the improvements made to the manuscript will meet the Reviewer's expectations.

Comment 1:

What is the actual use of the newly developed biomedical β-Ti alloy? It is noted that different service environment and requirements should be selected for evaluation of orthopaedic and dental materials. Please present the research objective in the section Introduction. If the present Ti alloy is designed for the development of artificial joint, the Co-Cr-based alloys should be used for comparisons.

Response:

Many thanks for pointing this out. This developed β-Ti alloy is designed **for orthopaedic implant applications** (rather than for dental implant). This is also why the cytocompatibility was assessed

using the MC3T3-E1 preosteoblast cells (relevant to bone-tissue interactions). In response, we have clarified this research objective in the *Introduction* and *Abstract* to highlight the intended biomedical context.

Regarding the benchmark material, we agree that Co-Cr-based alloys are widely used in artificial joint applications. However, the primary objective of this study is to develop an advanced β-Ti alloy that could potentially replace the widely adopted Ti-6Al-4V alloy as Ti64 remains the gold-standard alloy for orthopaedic implants and thus provides an essential baseline for evaluating new alloy developments. Meanwhile, it is also worth noting that the designed β-Ti alloy exhibits a substantially lower Young's modulus than both Ti–6Al–4V and Co–Cr alloys (as shown in Figure 5b), highlighting its advantage in reducing stress shielding and improving bone compatibility.

Revision: (Page 3)

Metals and alloys play an indispensable role in modern clinical practice, offering a unique combination of mechanical strength, biocompatibility, and corrosion resistance—traits essential for long-term load-bearing orthopaedic implants[1,2]. However, the elastic moduli of conventional biomedical implant alloys such as 316L stainless steel (~190 GPa), Co-Cr-Mo alloy (~220 GPa), and Ti-6Al-4V (Ti64) alloy (~110 GPa) are significantly higher than that of human cortical bone (~10–30 GPa)[3]. This stiffness mismatch disrupts physiological load transfer, leading to localized bone resorption and eventual implant loosening. In response to this challenge, β-Ti alloys have garnered increasing clinical attention due to their lower elastic modulus (~30–80 GPa), superior biomechanical compatibility, and greater flexibility[4]. Furthermore, additive manufacturing (AM) expands the potential of β-Ti alloys in orthopaedic implant applications by allowing precise control over porosity, mechanical properties, and surface topography, which are critical for osseointegration and long-term clinical success.

Comment 2:

How to calculate the non-equilibrium solidification behaviour including growth restriction factor (GRF), solidification freezing range (SFR), and hot-cracking susceptibility (HCS)? The calculated values of Ti-15.8Nb-9.2Ta-10.0Zr-7.7Sn and Ti64 alloys should be used to compare with the experimental results, which can support that the GRF, SFR, and HCS values can be used for prediction of printability.

Response:

We are sorry that the explanation to the CALPHAD simulation process is not detailed enough. The

non-equilibrium solidification simulations were implemented using the Thermo-Calc software with a TCTI4 database. The Scheil model was adopted because it assumes an ultra-high solidification rate, enabling the evaluation of solidification behavior under additive manufacturing conditions. Those alloy design metrics—including the solidification freezing range (SFR), growth restriction factor (GRF), and hot-cracking susceptibility (HCS)—were then extracted from the Scheil solidification curves using the established formulations (as shown in the Supplementary Equation S1-S3). For ensure reproducibility, a detailed explanation to the CALPHAD simulation process and the applied parameters has been provided in the Supplementary Information.

Regarding the experimental validation of the alloy design metrics, it should be noted that directly measuring non-equilibrium solidification behavior is not feasible due to the ultra-high cooling rates of LPBF (~10^6 K/s). CALPHAD-based Scheil simulations, as a result, provide a widely recognized approach for assessing such behavior, as they allow reliable extrapolation of multicomponent thermodynamics from well-characterized binary and ternary systems. Similar strategies have been successfully employed in previous studies to estimate hot-cracking susceptibility and solidification characteristics across various alloy systems (as shown in Refs. 1–5). In the present work, the experimentally observed good printability, defect-free as-built microstructure, and favorable mechanical properties of the ANTZS alloy further support the predicted GRF, SFR, and HCS values, confirming the robustness and reliability of our alloy design framework.

Supporting References

[1] Nartu, M. S. K. Y., *et al.*, *Nat. Commun.* **14**, 3288 (2023).

[2] Wakai, A., *et al.*, *Nat. Commun.* **16**, 1446 (2025).

[3] Sheikh, S., *et al.*, *npj Comput. Mater.* **11**, 179 (2025).

[4] Alabort, E., *et al.*, *Acta Mater.* **178**, 275–287 (2019).

[5] Tang, Y. T., *et al.*, *Acta Mater.* **202**, 417–436 (2021).

Revision: (Supplementary Information, Page 4)

For the CALPHAD simulations, titanium (Ti) was selected as the base element, with niobium (Nb) and tantalum (Ta) varied from 0 to 30 wt.% in 6 wt.% increments, and zirconium (Zr) and tin (Sn) varied from 0 to 10 wt.% in 5 wt.% increments. In total, 320 compositions were calculated using the Scheil module in the Thermo-Calc software with the TCTI4 database. The classical Scheil solidification model was adopted and all elements were treated as normal elements without fast diffusers. The solidification freezing range (SFR), hot cracking susceptibility (HCS), and growth restriction factor (GRF) data were extracted from the Scheil curves based on the Equation S1–S3.

The corresponding schematic diagram is provided in Figure S1.

$$SFR = T_{max} - T_{min} \quad \text{(S1)}$$

$$HCS = \frac{t(x = 0.9) - t(x = 1.0)}{t(x = 0.4) - t(x = 0.9)} \quad \text{(S2)}$$

$$GRF = \left| \frac{y(x = 0.05) - y(x = 0)}{0.05} \right| \quad \text{(S3)}$$

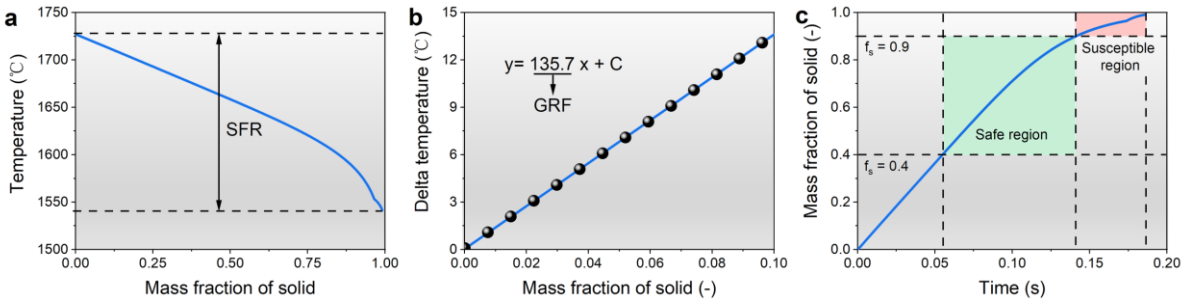

Figure S1. A thermodynamic calculation example based on the Scheil model. a Solidification freezing range (*SFR*). **b** Hot cracking susceptibility (*HCS*). **c** Growth restriction factor (*GRF*).

Comment 3:

Please provide the data used in the ML calculation for verification.

Response:

We thank the Reviewer for the careful comment. The source code and the running results have been uploaded to the Figshare platform for review purposes. The link is: https://figshare.com/s/004809cbf028a5204f89. Due to the restrictions imposed by the *Thermo-Calc End User License Agreement* (EULA), we are not able to make the dataset publicly available in the current stage. Nevertheless, we would be happy to share the related code used for analysing the raw data to others for research purpose upon request.

Revision: **(Page 23)**

Data availability

The data generated in this work is available within the article and its Supplementary Information. Source data are provided with this paper. Due to the restrictions imposed by the Thermo-Calc End User License Agreement (EULA), the CALPHAD data can only be shared upon reasonable request. Detailed procedures of the CALPHAD simulations used to reproduce the findings of this study are provided in the Supplementary Information.

Comment 4:

The authors used a 3.5 wt.% NaCl solution for the corrosion tests. Generally, electrochemical corrosion measurements of biomedical materials are performed in the 0.9 wt.% NaCl solution, instead of 3.5 wt.% NaCl solution. Please give the experimental results in the 0.9 wt.% NaCl solution.

Response:

We agree with the Reviewer that the 0.9 wt.% NaCl solution is a more reasonable solution for simulating the physiological environment. In response, the electrochemical corrosion measurements have been retested using the 0.9 wt% NaCl solution, as shown below.

Revision: (Supplementary Information, Page 18-19)

Figure S17a–c compares the electrochemical corrosion behaviour of LPBF-fabricated Ti64 and ANTZS alloys in 0.9 wt% NaCl solution. The results have been provided in Table S5. The polarization curves in Figure S17a show that the LPBF ANTZS alloy exhibits a slightly more negative corrosion potential (Ecorr) and a slightly higher corrosion current density (icorr) than Ti64, indicating a slightly higher corrosion rate. Specifically, the corrosion current densities for the LPBF-built ANTZS and Ti64 alloys are 0.0215 and 0.0113 μA cm^{-2}, respectively. Consistently, the Nyquist plots in Figure S17b reveal a smaller semicircle diameter for ANTZS, corresponding to a lower charge-transfer resistance (R_t) and thus a less protective passive film. The Bode plots in Figure S17c further confirm this trend, as ANTZS displays a lower impedance magnitude (|Z|) across the frequency range, although both alloys maintain a capacitive phase angle of about 70–80° (Figure S17d), suggesting that each forms a stable TiO_2-based oxide film. Overall, the results indicate that Ti64 possesses slightly superior corrosion resistance compared with ANTZS. The slightly lower corrosion resistance observed for LPBF ANTZS likely originates from factors not captured by the composition-only ML inputs, such as: (i) difference in passive-film nucleation and growth kinetics associated with β-dominated ANTZS versus α′-dominated Ti64; (ii) LPBF-induced texture and residual stress; and (iii) minor porosity difference. Nevertheless, note that the LPBF ANTZS alloy also exhibits a very low corrosion density of 0.0215 μA·cm^{-2} (comparable to 0.0113 μA·cm^{-2} for LPBF Ti-6Al-4V). Nevertheless, the ANTZS still demonstrates sufficient passivation and mechanical uniformity for biomedical applications.

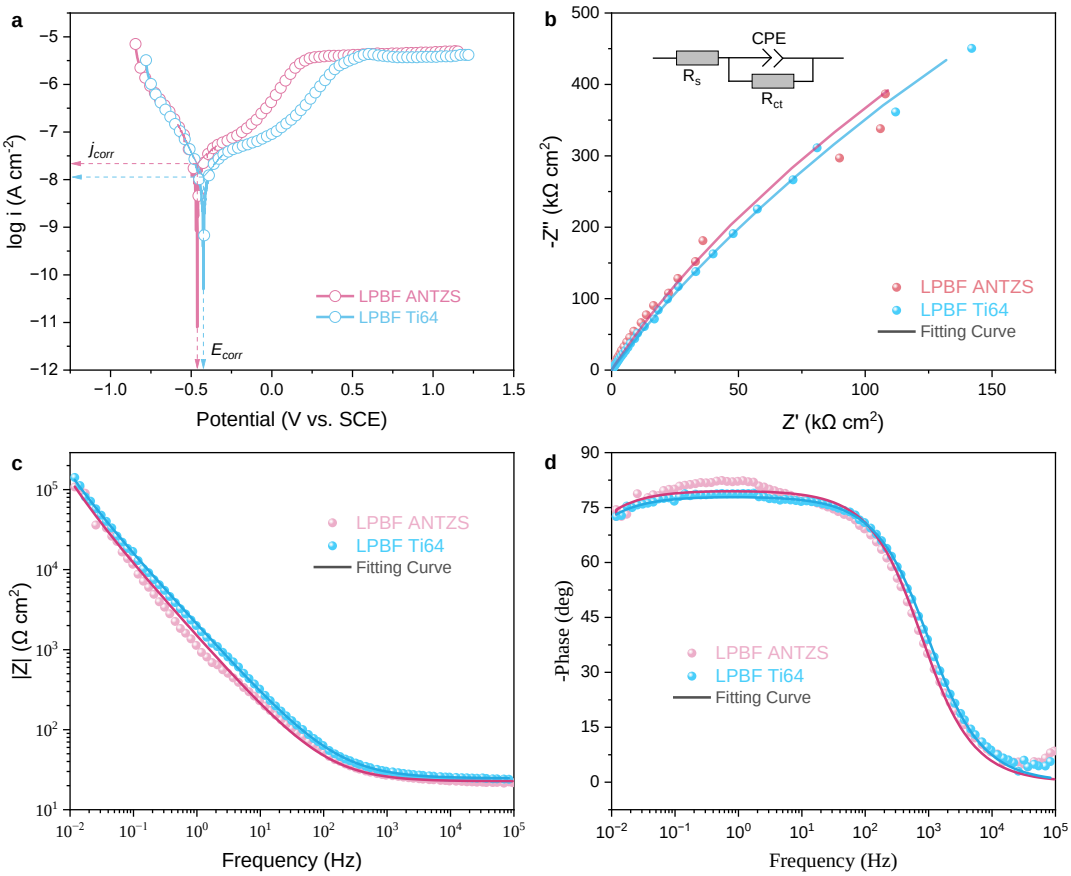

Figure S17. Comparative electrochemical corrosion behavior of LPBF ANTZS and Ti64 alloys. **a** Potentiodynamic polarization curves of the LPBF ANTZS and LPBF Ti64 alloys in 0.9 wt% NaCl solution. **b** Nyquist plots from electrochemical impedance spectroscopy (EIS). **c** & **d** Bode plots of impedance magnitude and phase angle derived from EIS measurements.

Comment 5:

The relationship among the YS, SFR, Ip, HCS, and BF is very complex, not simple linear. Therefore, I cannot understand the objective functions to maximise YS, SFR, and Ip, and to minimize HCS and BF in the multi-objective optimisation. Please explain it.

Response:

We thank the Reviewer for pointing this out. The relationships among YS, SFR, Ip, HCS, and BF are highly nonlinear and complex. As a result, a multi-objective genetic algorithm (NSGA-II) was employed to handle nonlinear, conflicting objectives within a high-dimensional design space. For the multi-objective optimisation problems, it is necessary to define the optimisation direction for each objective to identify Pareto-optimal solutions. **By stating "maximize" or "minimize", we indicate the intended optimisation direction for each objective, i.e., enhancing YS, SFR, and**

Ip while reducing HCS and BF, rather than implying that these objectives have linear relationships. The NSGA-II algorithm then searches the high-dimensional compositional space and constructs a Pareto front that represents the best possible trade-offs among these complex and competing objectives. In response, this clarification has also been integrated into the revised manuscript to avoid confusion to the readership.

Revision: **(Page 10)**

The NSGA-II algorithm is selected for its proven capability to efficiently approximate the Pareto front and maintain diversity among solutions[38]. The optimisation aims to obtain a set of Pareto-optimal compositions in which no single objective can be improved without compromising others. The optimisation problem is formulated with four decision variables representing the alloying element contents, each constrained within predefined limits (Nb and Ta $\in$ [0, 30]; Zr and Sn $\in$ [0, 10], wt%). The objectives are defined as improving *YS*, *SFR*, and *Ip*, while reducing *HCS BF* and, which corresponds with the objectives of enhancing strength, reducing mechanical anisotropy, increasing corrosion resistance, improving printability, and lowering Young's modulus.

Comment 6:

The Ti-15.8Nb-9.2Ta-10.0Zr-7.7Sn alloy has higher corrosion-current density than Ti64 alloy. Does this result indicate that the ML calculations fail in the corrosion property? Maybe the electrochemical impedance spectroscopy test can be performed for these two alloys.

Response:

Many thanks to the Reviewer to this careful comment. Our ML surrogate for corrosion uses the peak anodic current density (I_p) predicted from the electronic descriptor bond order (*Bo*), following the model originally established by Okazaki et al. (*Mater. Trans. JIM, 1994*), which correlates a higher *Bo* with lower anodic dissolution rates. In this work, the slightly lower corrosion resistance observed for ANTZS likely originates from factors not captured by the composition-only ML inputs, which could include: (i) difference in passive-film nucleation and growth kinetics associated with β-dominated ANTZS versus α′-dominated Ti64; (ii) LPBF-induced texture and residual stress; and (iii) minor porosity difference. Nevertheless, note that the LPBF ANTZS alloy also exhibits a very low corrosion density of 0.0215 $\mu A \cdot cm^{-2}$. According to *ASTM G102-23 Standard*, these values correspond to corrosion rates of approximately 0.19 $\mu m \cdot year^{-1}$ (ANTZS) and 0.10 $\mu m \cdot year^{-1}$ (Ti64), respectively, indicating both alloys are well within the limits required for orthopaedic implant applications.

Additionally, note that the corrosion resistance is one of the five objectives (alongside BF, SFR, HCS and YS) in the multi-objective optimisation framework. As more weight is assigned to BF to achieve a bone-like low modulus, corrosion resistance serves as a balanced objective rather than the dominant one. Consequently, the final ANTZS composition represents a Pareto-optimal trade-off that priorities low modulus, while maintaining good printability, clinically acceptable strength and corrosion performance. Therefore, the electrochemical testing results are fully consistent with the intended optimisation strategy rather than indicative of ML prediction failure.

Regarding with the electrochemical impedance spectroscopy (EIS) test, we fully agree with the Reviewer that EIS test can offer more complementary information to the corrosion behavior. As a result, EIS analyses has been supplemented, as shown below.

Revision: **(Page 19)**

Figure S17 presents the comparison of the electrochemical corrosion behaviour of LPBF ANTZS and Ti64 alloys through polarization and EIS tests in the 0.9 wt % NaCl solution, with the results summarised in Table S5. Overall, the LPBF Ti64 exhibits slightly superior corrosion resistance than the LPBF ANTZS, as reflected by its lower corrosion current density (i_{corr} = 0.0113 μA·cm^{-2}) and higher charge-transfer resistance (R_{ct} = 5.15 × 10^6 Ω), compared with the LPBF ANTZS alloy (i_{corr} = 0.0215 μA·cm^{-2}, R_{ct} = 4.35 × 10^6 Ω). The slightly lower corrosion resistance of LPBF ANTZS may be attributed to factors not fully captured by composition-only ML predictions, including differences in passive-film nucleation and growth kinetics between β-dominated ANTZS and α′-dominated Ti64, as well as LPBF-induced residual stresses and minor porosity variations. Nevertheless, the consistent trends observed across the polarization curves and impedance spectra further corroborate that both alloys exhibit stable passive behaviour and excellent corrosion resistance in physiological environments.

(Page 22)

Electrochemical corrosion measurement

Electrochemical tests were conducted using a CHI electrochemical workstation in a conventional three-electrode configuration. The alloy specimens were mounted as the working electrode with an exposed area of approximately 1 cm², while a saturated calomel electrode (SCE) and a platinum mesh were employed as the reference and counter electrodes, respectively. All measurements were performed in 0.9 wt% NaCl solution at room temperature. The open-circuit potential (OCP) was tested for 30 min before measurements. EIS tests were performed at OCP using a 5 mV sinusoidal voltage perturbation in the frequency range of 10 kHz to 0.01 Hz, with logarithmic spacing of 10

points per decade. Potentiodynamic polarization curves were obtained by sweeping the potential from OCP − 0.5 V to OCP + 1.8 V at 1 mV·s^{-1}.

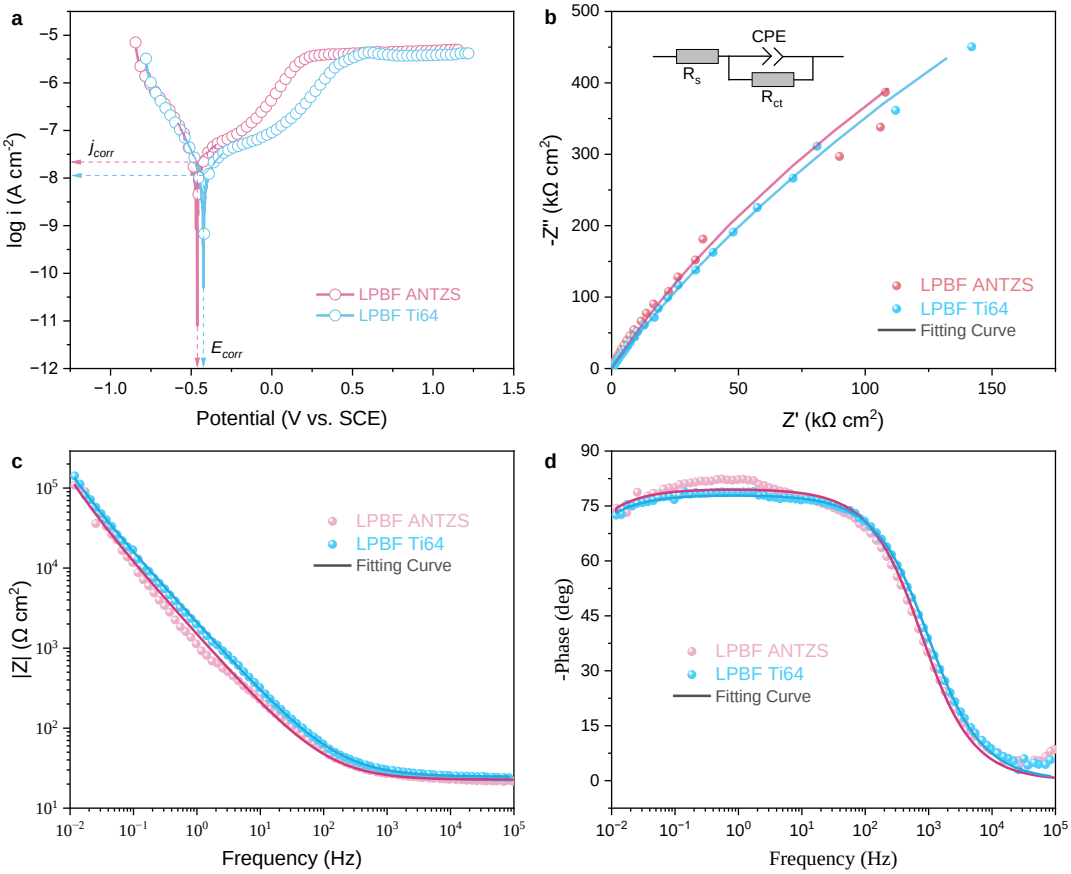

Figure S17. Comparative electrochemical corrosion behavior of LPBF ANTZS and Ti64 alloys. a Potentiodynamic polarization curves of the LPBF ANTZS and LPBF Ti64 alloys in 0.9 wt% NaCl solution. **b** Nyquist plots from electrochemical impedance spectroscopy (EIS). **c** & **d** Bode plots of impedance magnitude and phase angle derived from EIS measurements.

Reviewer #2

General comment:

This work presents a machine-learning (ML)-driven computational framework for discovering AM-specific biomedical β-Ti alloy compositions with low-modulus, optimized printability, mechanical and corrosion properties, and biocompatibility. Using this framework, a new AM-specific Ti-Nb-Ta-Zr-Sn (ANTZS) alloy was correspondingly designed and validated via laser powder bed fusion (LPBF). ***The manuscript is very well organized and well written.*** *While the concept of machine learning has been reported in the literature, preparing medical metals for 3D printing is still novel. Please find my comments as follow:*

Response:

We thank the Reviewer very much for recognizing our work and appreciate all the valuable comments. In response, we have refined the title, clarified the alloy design framework with more details, improved the clarity of figures, and supplemented additional experiments, etc. We hope that our responses and the improvements made to the manuscript will meet the Reviewer's expectations.

Comment 1:

BF is suitable for predicting the elastic modulus of β-titanium alloys, but not for all medical metal materials. The framework can be just used to design 3D β-titanium alloys with low elastic modulus. So, I suggest the author consider optimizing the title of manuscript.

Response:

We agree that our ML-driven computational framework is specifically aimed at designing β-titanium alloys for additive manufacturing. Following the suggestion, we have refined the title to "*Machine Learning-Driven Discovery of Advanced Biomedical Titanium Alloys for Additive Manufacturing*" to more accurately reflect the focus of this work

Revision: (Title)

"*Machine Learning-Driven Discovery of Advanced Biomedical Titanium Alloys for Additive Manufacturing*"

Comment 2:

The author mentioned "The alloy composition sets include Ti as the base element, with Nb and Ta varying from 0 to 30 wt.% (in increments of 6 wt.%), and Zr and Sn varying from 0 to 10 wt.% (in increments of 5 wt.%).", Why set such a component interval?

Response:

We thank the Reviewer for pointing this out. The selection of the compositional intervals was based on the following considerations:

(1) Rationale for the composition ranges

The selection of the composition range is based on metallurgical and practical considerations. Nb and Ta are well-established β-stabilizers in Ti alloys. To design a metastable β-Ti alloy with moderate Mo_{eq} and moderate cost, their contents were limited to a maximum of 30 wt%. For Zr and Sn, it should be noted that their most effective compositional range on modulus reduction, ductility enhancement, and biocompatibility manifest is typically below 10 wt% (The typical Zr and Sn-

containing biomedical β-Ti alloys generally contain Zr and Sn below 10 wt%, e.g., Ti-29Nb-13Ta-4.6Zr, Ti-35Nb-7Zr-5Ta and Ti-25Nb-8Sn alloys). Excessive Zr and Sn (> 10wt%) may lead to undesirable brittle ω, Ti_2Sn or Ti_3Sn phases, which are highly undesirable for biomedical implant applications.

(2) Rationale for the increments

The increments (6 wt% for Nb/Ta and 5 wt% for Zr/Sn) were chosen to balance resolution with computational efficiency. A finer step size would dramatically expand the compositional design space, making CALPHAD-based simulations more time-consuming. By selecting these increments, the main compositional trends can be effectively captured while keeping the dataset manageable for high-throughput CALPHAD simulations.

We have further clarified the above discussions into the revised manuscript, as shown below.

Revision: **(Page 5)**

Figure 1 presents the schematic of the proposed alloy design framework, which integrates ML, physical modelling, and multi-objective optimisation. Firstly, a design-of-experiments (DoE) table was constructed to define the initial set of alloy compositions. In this study, Nb and Ta were varied from 0 to 30 wt.% in 6 wt.% increments, while Zr and Sn were varied from 0 to 10 wt.% in 5 wt.% increments. The upper limits for Nb and Ta (30 wt.%) were selected to ensure adequate β-phase stability without imposing excessive density or cost. Similarly, the upper limits for Zr and Sn (10 wt.%) were chosen based on their most effective ranges for lowering elastic modulus and improving biocompatibility, while preventing the formation of brittle phases (e.g., ω, Ti_2Sn, Ti_3Sn)[17]. The selected composition increments (6 wt.% for Nb/Ta and 5 wt.% for Zr/Sn) were designed to strike a balance between capturing essential metallurgical trends and keeping the CALPHAD calculations computationally manageable.

Comment 3:

Generally speaking, the larger the SFR is, the more likely solidification cracks occur. In the model of this article, how to balance the contradiction between nucleation rate and cracks?

Response:

We thank the Reviewer for pointing this out. Although it is often assumed that a larger solidification freezing range (SFR) corresponds to a higher risk of solidification cracking—because a larger SFR implies a longer solidification time under a given cooling rate—this relationship is not necessarily direct. **This is because solidification cracking only occurs during the terminal stage of**

solidification, when the solid fraction is very high (e.g., >90%) and the remaining liquid films no longer provide sufficient feeding. Therefore, in our alloy design framework, a more physically meaningful indicator, hot cracking susceptibility (HCS) is adopted to assess the cracking susceptibility. The HCS is defined as the ratio between the time required to solidify the final ~10% of liquid and the time required for the solid fraction to increase from 40% to 90%, based on the classical Clyne–Davies model. This is to say, the HCS specifically captures the late-stage solidification interval where hot cracking actually forms. In contrast, herein, the SFR is used to capture CET-related nucleation behaviour (FYI. https://doi.org/10.1038/s41467-023-38885-9). The multi-objective optimisation approach then balances these competing factors (i.e., SFR, HCS, YS, Ip, and BF) allowing the model to identify the optimal compositions that achieve an optimal compromise among all objectives.

Revision: **(Page 6)**

Considering the ultrahigh solidification rate of AM (10^5–10^7 K/s for LPBF[18]), the Scheil model was employed to simulate its non-equilibrium solidification behaviour of the alloys. Key physical properties related to non-equilibrium solidification, including growth restriction factor (*GRF*), solidification freezing range (*SFR*), and hot-cracking susceptibility (*HCS*), were evaluated. Among them, the *GRF* exhibits an inverse relationship with grain size, thereby influencing grain boundary strengthening and mechanical strength[19,20]. A larger *SFR* promotes higher undercooling and nucleation rates, which suppresses columnar growth, ultimately improving mechanical isotropy[21]. Besides, as solidification cracking is controlled predominantly by the terminal stage of solidification, the *HCS* is evaluated following the classical Clyne-Davies model, defined as the ratio between the time required to solidify the final ~10% of liquid and the time required for the solid fraction to increase from 40% to 90%[22]. Reducing *HCS* is thus essential to ensure defect-free manufacturing and robust printability.

Comment 4:

In section 2.3, where are the objective functions YS, SFR, Ip, HCS and BF? Where is GRF?

Response:

The objective functions have been provided in the section "*Physical models for composition-properties relations*" before the previous section 2.3. The GRF has been integrated into the grain boundary strengthening model, as shown in the Equation (6) & (7) in the manuscript. In order to improve clarity, we have further clarified this in the main text.

Revision: **(Page 10)**

Multi-objective optimisation and decision-making

In the previous section, five objective functions—*YS*, *SFR*, *Ip*, *HCS*, and *BF*—were formulated using physics-based models. To optimise these objectives, a multi-objective genetic algorithm (MOGA) approach based on the non-dominated sorting genetic algorithm II (NSGA-II) was employed to optimise the alloy composition considering multiple, potentially conflicting objectives, including metallurgical parameters, mechanical properties, and corrosion resistance[37].

Comment 5:

What do the color gradations in Figures 4a and 4b represent? Porosity?

Response:

The color scale in the previous Figure 4a and b (Figure 4c and d in the revised manuscript) represents the relative density (RD) of the alloys. To improve clarity, we have refined the color bar (and the related description in the figure title) in the revised figures.

Revision: **(Page 14)**

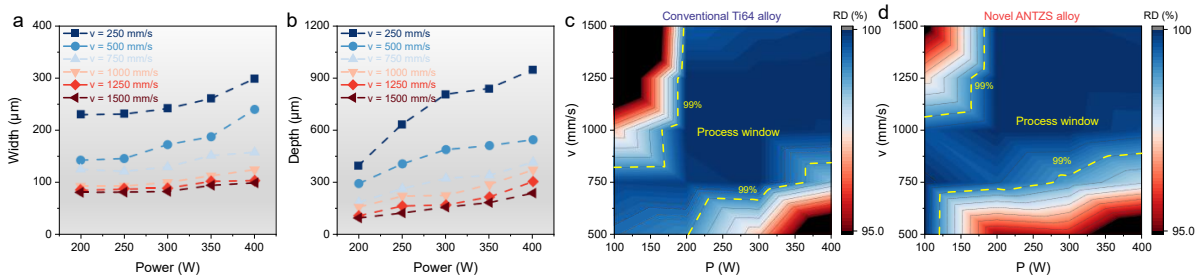

Figure 4. … **c Relative density (RD) of** LPBF-built Ti64 bulk samples processed under varying process parameters. **d RD of** LPBF-built ANTZS bulk samples under the same parameter set….

Comment 6:

Please provide the experimental evidence of ANTZS alloy with a smaller melt pool and smaller mushy zone compared to Ti64. What are the reasons for this phenomenon to occur?

Response:

Many thanks to the Reviewer for this careful comment. The differences in the simulated melt-pool dimensions arise from the distinct thermophysical properties of the two alloys, including their melting points, specific heat capacities, and thermal conductivities, which govern heat transfer and solidification behavior during laser melting. Consequently, the simulated melt pool and mushy zone

sizes differ significantly between the two alloys.

We conducted single-track LPBF printing experiments for the Ti64 alloy, as shown below (Figure R1). Notably, we found that **the single-track melt-pool morphology of Ti64 is almost illegible, because the martensitic transformation during LPBF seems eliminate the contrast normally used to identify melt pool boundaries**. This makes direct measurement of the melt pool size of Ti64 infeasible. One potential alternative could be to print Ti64 powder on a wrought Ti64 substrate (instead of a 3D-printed one) to enable melt pool observation. However, in that case, the laser absorptivity—and consequently the melt pool size—would be strongly affected by the surface roughness of the wrought substrate, resulting in unrealistic and non-comparable data. **As a result, after careful considerations, we have removed the single-track simulation results to ensure the rigor of this work.** We hope it can meet with the Reviewer's approval.

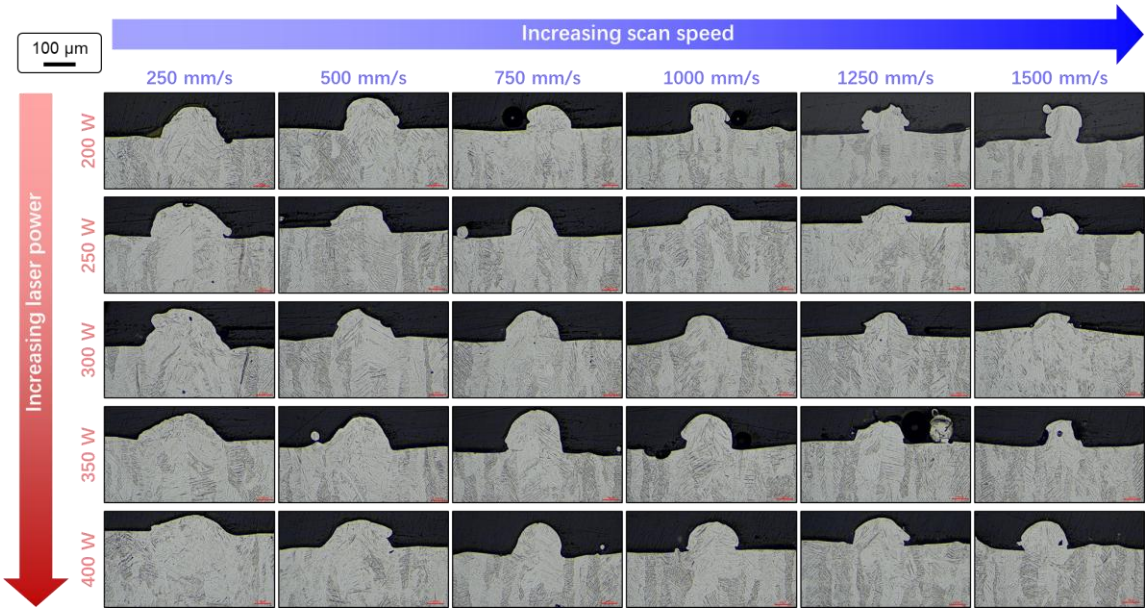

Figure R1. OM images of single-track LPBF-built Ti64 alloy under varying laser powers and scan speeds. (Note that the *melt pool morphology of Ti64 single-track is not visible* because the martensitic transformation during LPBF eliminates the contrast normally used to identify melt pool boundaries.)

Revision: (Page 12-13)

To validate the alloy design framework, the optimal ANTZS alloy was first synthesized by casting, followed by the preparation of pre-alloyed powder using gas atomisation. The pre-alloyed powder was then processed via LPBF to fabricate the samples. Firstly, single-track printing was used to screen the process parameters preliminarily. Initial experiments focused on analysing variations in melt pool width (Figure 4a) and depth (Figure 4b) under different processing parameters. Based on

these single-track results, bulk ANTZS samples were fabricated within a reasonable energy density range at laser powers of 100–400 W and scan speeds of 500–1500 mm/s (Figure S7). For comparison of printability, Ti64 alloy samples were printed under the same process parameters (Figure S8). Overall, the ANTZS alloy exhibits a slightly wider process window (relative density >99%) than Ti64, as shown in Figure 4c and d. Notably, ANTZS shows reduced sensitivity to keyhole pore formation in the high energy density region (lower right region of Figure 4c and d). This behavior can be attributed to differences in thermophysical properties (e.g., melting point, specific heat capacity, and thermal conductivity) which collectively govern heat transfer and solidification during laser melting.

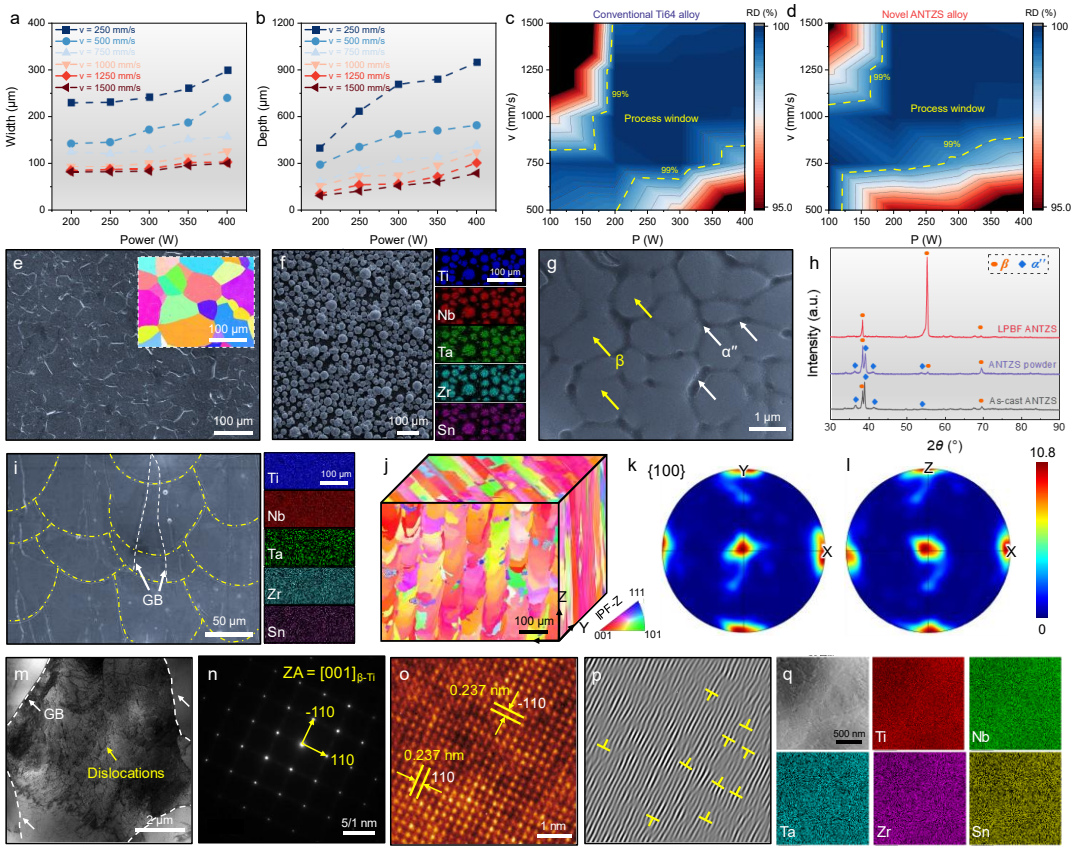

Figure 4. Printability and microstructure characteristics. a Single-track melt pool width of the ANTZS alloy under varying process parameters. **b** Single-track melt pool depth of the ANTZS alloy under varying process parameters. **c** Relative density (RD) of LPBF-built Ti64 bulk samples processed under varying process parameters. **d** RD of LPBF-built ANTZS bulk samples under the same parameter set. **e** SEM image of the as-cast ANTZS alloy (inset: IPF orientation map). **f** SEM image and EDS mappings of the ANTZS powder, **g** internal microstructure of the ANTZS powder. **h** XRD patterns. **i** SEM image and EDS mappings of the LPBF-built ANTZS alloy (fabricated under the optimal process parameter: laser power of 400 W and scan speed of 750 mm/s). **j** Three-

dimensional IPF orientation maps of the LPBF-built ANTZS alloy. **k** {100} pole figure along xy plane. **l** {100} pole figure along xz plane. **m** bright-field TEM image of LPBF-built ANTZS alloy. **n** SAED pattern. **o** & **p** HRTEM images. **q** STEM-EDS micro-scale elemental mappings.

Comment 7:

The arrows in Figure 4i were not the Fusion Line. Please use an arrow to indicate the β-grains.

Response:

Many thanks for this careful comment. Revised as suggested.

Comment 8:

Is the external force of the tensile test applied parallel to the building direction or perpendicular to the printing direction?

Response:

Many thanks for this careful comment. The tensile tests presented in Figure 5 are tested along the build direction. The tested results along the transverse direction are presented in Figure S9.We have further clarified this in the figure caption.

Revision: **(Page 16)**

Figure 5. Mechanical properties evaluation. a Engineering stress-strain curves (LPBF ANTZS is tested along the build direction). **b** Comparison of LPBF-built ANTZS….

Comment 9:

After the ML calculation, the author chosen one ANTZS composition to conduct the verification experiments, how did the authors balance printability and performance? Just chose one composition to conduct the verification experiments, is the quantity too small?

Response:

Many thanks to the Reviewer for pointing this out. One key contribution of our work is the integration of multi-objective optimisation into the alloy design framework. Within this framework, printability and performance—including mechanical properties, biocompatibility, and corrosion resistance—are balanced by evaluating trade-offs among multiple thermophysical properties in conjunction with physics-based models.

Regarding the selection of only one single composition for experimental validation, the primary reason is the long manufacturing lead time and high cost of producing pre-alloyed powders. In

addition, Nb and Ta are highly refractory elements, making in-situ alloying via additive manufacturing (i.e., using blended elemental powders) impractical. Consequently, we employed the TOPSIS decision-making method to identify the composition with the most balanced properties for validation. As shown in Supplementary Figure S5, the selected composition demonstrates superior overall performance within the Ti-*x*Nb-*y*Ta-*z*Zr-*w*Sn alloy space (x = 0–30 wt%, y = 0–30 wt%, z = 0–10 wt%, w = 0–10 wt%). For these reasons, only this composition was chosen as a representative solution for experimental validation, and we have clarified this rationale in the main text.

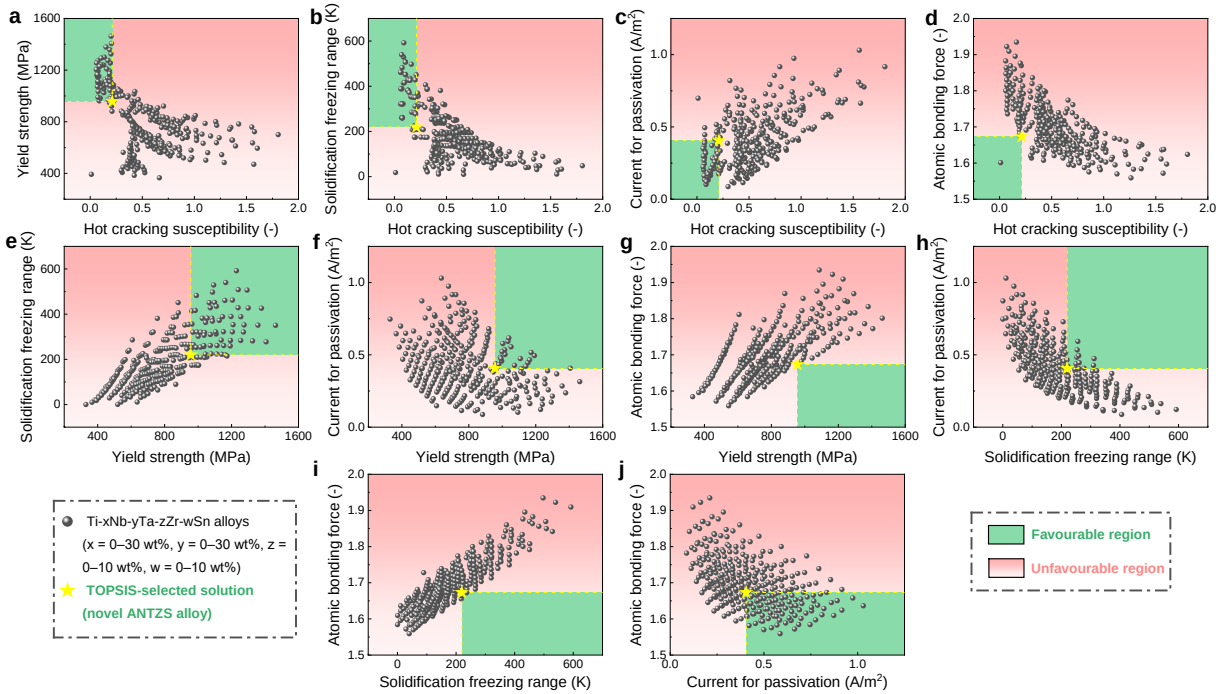

Figure S5. Comprehensive properties of the newly developed ANTZS alloy compared to all the Ti-*x*Nb-*y*Ta-*z*Zr-*w*Sn alloy composition space (within the composition range of x = 0–30 wt%, y = 0–30 wt%, z = 0–10 wt%, and w = 0–10 wt%). ……

Revision: (Page 10)

The NSGA-II algorithm was selected for its proven capability to efficiently approximate the Pareto front and maintain diversity among solutions[38]. The MOGA aimed to obtain a set of Pareto-optimal compositions in which no single objective can be improved without compromising others. The optimisation problem was formulated with four decision variables representing the alloying element contents, each constrained within predefined limits (Nb and Ta ∈ [0, 30]; Zr and Sn ∈ [0, 10], wt%). The objectives are defined as improving *YS*, *SFR*, and *Ip*, while reducing *HCS* and *BF*, which corresponds with the objectives of enhancing strength, reducing mechanical anisotropy, increasing corrosion resistance, improving printability, and lowering Young's modulus.

(Page 11)

To select the representative composition for experimental validation, the technique for order of preference by similarity to ideal solution (TOPSIS) method was then employed as the decision-making tool to identify the optimal composition that simultaneously balances printability, mechanical performance, biocompatibility and corrosion resistance.

(Page 11)

The 3D plots in Figure 3b and c illustrate that the developed ANTZS alloy exhibits superior comprehensive properties across the vast compositional space. A more straightforward two-dimensional comparison of various objectives is shown in Figure S5, which indicates that the selected ANTZS alloy outperforms other candidates within the Ti-*x*Nb-*y*Ta-*z*Zr-*w*Sn alloy space (x = 0–30 wt%, y = 0–30 wt%, z = 0–10 wt%, w = 0–10 wt%) and is therefore chosen for experimental validation.

Comment 10:

Why was Ti6Al4V used for comparison in this study instead of other beta titanium alloys?

Response:

We appreciate the Reviewer's thoughtful comment. The primary reason for selecting Ti64 for comparison is that it remains the most widely adopted titanium alloy in clinical orthopedic applications and is still regarded as the benchmark ('gold standard') for biomedical implants. Using Ti64 provides a clinically relevant baseline and enables the performance of the newly designed alloy to be directly compared with the material that dominates both current medical practice and the additive manufacturing literature. This ensures that the advantages of the ANTZS alloy can be readily appreciated by the broader biomedical and AM communities.

Notably, while Ti64 was chosen as the primary reference, we also benchmarked ANTZS against other AM-fabricated β-Ti alloys. As shown in Figure 5b, ANTZS exhibits an excellent combination of low elastic modulus and high ductility compared to a range of state-of-the-art commercial β-Ti alloys. This demonstrates that ANTZS not only outperforms the clinical gold standard (Ti64) but also surpasses the best available AM-built β-Ti alloys reported in the literature.

Revision: **(Page 21)**

Additionally, LPBF-fabricated Ti64 alloy was adopted as the control group, as Ti64 remains the gold-standard alloy for orthopaedic implants and thus provides an essential baseline for evaluating new alloy developments.

Comment 11:

There are two (C) in the title of Figure 4.

Response:

Many thanks to the Reviewer for pointing this out. We have revised it accordingly and performed a careful double-check to avoid minor error.

Revision: **(Page 14)**

Figure 4. Printability and microstructure characteristics. a Single-track melt pool width of the ANTZS alloy under varying process parameters. **b** Single-track melt pool depth of the ANTZS alloy under varying process parameters. **c** Relative density (RD) of LPBF-built Ti64 bulk samples processed under varying process parameters. **d** RD of LPBF-built ANTZS bulk samples under the same parameter set……

Comment 12:

Why does the as-cast alloy undergo a phase transformation during the tensile, while the printed alloy does not? Is there a significant difference in the elastic modulus between the two alloys?

Response:

The different deformation beahvior between as-cast and LPBF ANTZS can be mainly attributed to their distinct microstructural characteristics. The as-cast ANTZS alloy exhibits a dual-phase microstructure consisting of α″ and β phases. During tensile deformation, the softer α″ phase deforms preferentially at the initial stage. Upon sufficient deformation of α″, localized stress accumulation within the β matrix, along with the cooperative deformation between the two phases, promotes a strain-induced β → α″ transformation, resulting in a double-yielding phenomenon. We have supplemented a discussion, and XRD and EBSD analysis is also supplemented into the revised manuscript to strengthen this explanation. In contrast, the LPBF-built ANTZS alloy displays a relatively finer single-phase β microstructure due to the ultrafast cooling rate. This structure significantly increases yield strength and enhances β phase stability, thereby suppressing the stress-induced martensitic transformation.

Regarding the elastic modulus, the LPBF-built alloy exhibits a slightly lower modulus compared to the as-cast counterpart (Supplementary Table S4). This difference can be mainly attributed to the pronounced <001>//BD texture in the LPBF sample, which corresponds to a lower modulus direction in the cubic lattice due to weaker atomic bonding. Relevant clarifications and revisions have been incorporated into the manuscript as indicated below.

Revision: **(Page 15)**

Figure 5a presents the engineering stress-strain curves of the LPBF-built ANTZS alloy printed under optimal process parameters (i.e., P = 400 W, v = 750 mm/s), with the results summarised in Table S4. Notably, the strength and ductility of the LPBF-built ANTZS alloy are both superior than its as-cast counterpart. This improvement can be attributed to microstructural refinement and the formation of a metastable β-phase microstructure during the rapid solidification associated with LPBF. In contrast, the as-cast ANTZS alloy exhibits a typical double-yielding phenomenon, which can be attributed to the cooperative deformation of α″ and β phases and the strain-induced β → α″ martensitic transformation (Figure S15). More importantly, compared to other state-of-the-art AM-built biomedical alloys (including Ti alloys, stainless steels, NiTi alloys, Mg alloys, Zn alloys, CoCrMo alloys, pure Ta), the LPBF-built ANTZS alloy (prepared under optimal process parameters) exhibits a great combination of low Young's modulus (42.7 ± 2.1 GPa) and high ductility (~30.9 ± 3.2%) (Figure 5b), demonstrating enhanced flexibility and highlighting its potential for orthopaedic implant applications.

(Supplementary Information, Page 17-18)

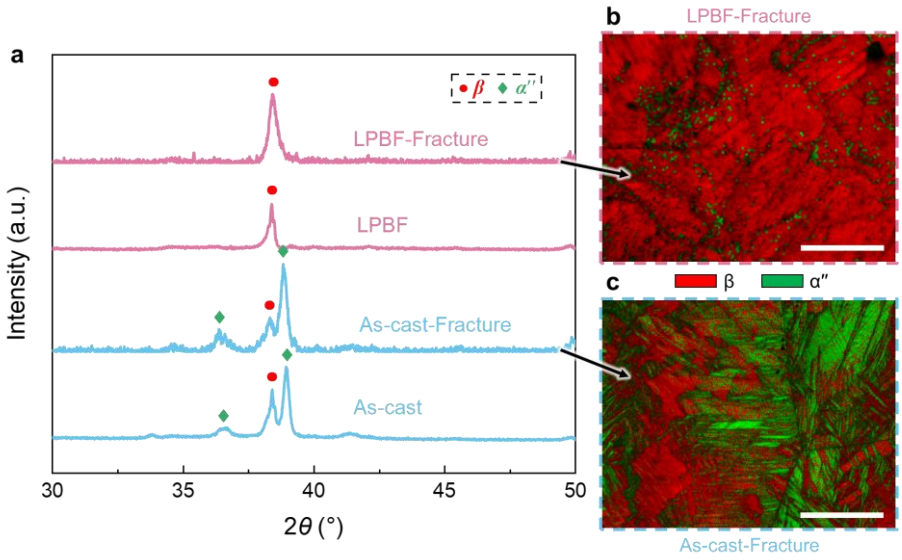

Figure S15. Comparison of phase transformation and microstructure evolution in as-cast and LPBF-built ANTZS alloys before and after fracture. a XRD patterns of the alloys in the as-cast, LPBF, and post-fracture states. **b** Phase map of the LPBF ANTZS after fracture. **c** Phase map of the as-cast ANTZS after fracture.

The different deformation behavior between as-cast ANTZS and LPBF ANTZS can be primarily attributed to their distinct microstructural characteristics. Figure S15a presents the XRD patterns of the as-cast and LPBF ANTZS alloys before and after tensile fracture. The as-cast ANTZS alloy is

consist of α″+β dual-phase microstructure. During tensile test, it can be induced that the softer α″ phase deforms and/or reorient first, followed by cooperative deformation and strain-induced β→α″ martensitic transformation, leading to the double-yielding behavior. Besides, the XRD patterns in Figure S15a show that the β peak intensity of the as-cast ANTZS decreases after fracture, confirming a strain-induced β → α″ martensitic transformation during tensile deformation. Correspondingly, the phase map of the as-cast alloy reveals extensive α″ formation after fracture (Figure S15c). In contrast, the LPBF-built alloy exhibits a single-phase β microstructure with finer grains, which stabilise the β phase and suppresses strain-induced martensitic transformation; this is reflected in both the nearly unchanged XRD pattern and the predominantly β-phase after fracture (Figure S15b).

Response to the Referees Letter

Title: *Machine Learning-Driven Discovery of Advanced Biomedical Titanium Alloys for Additive Manufacturing*

Manuscript number: *NCOMMS-25-48046A*

First, we sincerely thank the Reviewer for the careful evaluation of our manuscript and the constructive comments. In response, we have carefully revised the manuscript to address each point raised. All modifications are highlighted in yellow in the revised manuscript.

Reviewer #2
General comment: *The author answered almost all of my questions carefully, but there are two questions that need to be explained by the author before acceptance.* **Response:** We sincerely thank the Reviewer for recognizing our efforts. According to the comments, we have added further discussion in the revised version to clarify the relevant mechanisms.
Comment 1: *In the revised paper, the authors mentioned "During tensile test, it can be induced that the softer α″ phase deforms and/or reorient first, followed by cooperative deformation and strain-induced β→α″ martensitic transformation, leading to the double-yielding behavior." In fact, the elastic modulus of α″ is always higher than that of β, so α″ is not the softer. Moreover, before the first yielding, when stress is applied to both the β phase and the α″ phase simultaneously, the deformation of the α″ phase is smaller due to the higher elastic modulus of the hardened phase. From the moment of yielding, the martensitic phase transformation begins to activate. Why does the α″ phase deform and/or reorient first?* **Response:** We thank the Reviewer for this insightful comment. Based on a careful re-examination of the experimental results and the relevant literature, we recognize that the β phase is firstly to reach the onset of yielding due to its lower slip resistance in (α″ + β) dual-phase β-Ti alloys. As a result, the observed double-yielding behaviour (in the as-cast alloy) can be explained as follows: the first

yielding corresponds to the onset of plastic deformation of the β matrix, accompanied by activation of strain-induced β → α″ martensitic transformation. The second yielding is associated with the transition to more extensive plastic flow after a sufficient fraction of β has been transformed and the microstructure has been substantially hardened. In response, we have revised the related contents in the supplementary information, as shown below.

Revision: (Supplementary Information, Page 12)

As shown in Figure 5a, the as-cast ANTZS alloy exhibits a tensile deformation behavior distinctly different from that of the LPBF-built ANTZS alloy, characterized by a double-yielding phenomenon. This behavior originates from the α″ + β dual-phase microstructure of the as-cast alloy, in contrast to the single metastable β-phase microstructure of the LPBF-built alloy. XRD analysis in Figure S11a reveals a clear reduction in β-phase peak intensity after tensile fracture in the as-cast ANTZS alloy, indicating the occurrence of strain-induced martensitic transformation (β → α″) during tensile test. Consistently, EBSD phase mapping of the fractured as-cast ANTZS sample confirms extensive formation of strain-induced α″ martensite (Figure S11c). Prior to yielding, it can be inferred that both β and α″ phases elastically share the applied load, while the first yielding is primarily associated with irreversible deformation in the β matrix accompanied by the onset of β → α″ transformation. The progressive martensitic transformation and the resulting increase in β/α″ interfacial constraints enhance work hardening, giving rise to the double-yielding behavior. In contrast, the LPBF ANTZS alloy retains a predominantly single-phase β microstructure before and after fracture (Figure S11a and b), indicating suppressed strain-induced martensitic transformation and resulting in a smooth, single-yield tensile response.

Comment 2:

Authors also mentioned "Regarding the elastic modulus, the LPBF-built alloy exhibits a slightly lower modulus compared to the as-cast counterpart (Supplementary Table S4). This difference can be mainly attributed to the pronounced //BD texture in the LPBF sample, which corresponds to a lower modulus direction in the cubic lattice due to weaker atomic bonding." Elastic modulus is crucial for biomedical materials, but the interpretation of elastic modulus in as-cast and LPBF alloys is still insufficient. Besides the texture, the phase composition, β, and porosity of LPBF alloys also affect the elastic modulus, compared to as-cast alloys, β+α". Please provide a more complete explanation.

Response:

We thank the Reviewer for this careful comment. We agree that the elastic modulus is governed by multiple microstructural factors rather than crystallographic texture alone. To provide a more comprehensive and rigorous interpretation, we have revised the related contents in the main text and the supplementary information to clarify the combined effects of crystallographic texture, phase constitution, and porosity, as shown below.

Revision: (Main Text, Page 15)

Figure 5a presents the engineering stress-strain curves of the LPBF ANTZS alloy fabricated under the optimal process parameters and the as-cast ANTZS alloy. Notably, the strength and ductility of the LPBF-built ANTZS alloy are both superior to its as-cast counterpart. This improvement can be attributed to microstructural refinement and the formation of a metastable β-phase microstructure during the rapid solidification associated with LPBF. In contrast, the as-cast ANTZS alloy displays a characteristic double-yielding behaviour, arising from strain-induced β → α″ martensitic transformation (Figure S11). Besides, the as-cast ANTZS alloy exhibits a higher Young's modulus than the LPBF-built ANTZS alloy (Table S4), primarily due to the combined effects of weaker crystallographic texture, the presence of α″ martensite, and the slight differences in porosity.

(Supplementary Information, Page 16)

Notably, with respect to elastic modulus, the differences among the SPS-fabricated, as-cast, and LPBF-built ANTZS alloys can be attributed to the combined effects of crystallographic texture, phase constitution, and porosity. The SPS ANTZS alloy exhibits an equiaxed grain structure with a relatively weak ⟨001⟩ texture, resulting in a more orientation-averaged elastic response and therefore a higher elastic modulus compared with the LPBF ANTZS alloy. Although the SPS sample also possesses a single β-phase microstructure, the absence of a strong low-modulus ⟨001⟩ texture limits further modulus reduction. In contrast, the as-cast ANTZS alloy contains an α″ + β dual-phase microstructure, in which the presence of α″ martensite intrinsically increases the overall elastic modulus. For the LPBF-built ANTZS alloy, the synergy of a strong cubic ⟨001⟩ texture, a single metastable β-phase microstructure, and minor process-induced keyholing porosity contributes to the lowest elastic modulus among the three processing routes.